

Center vortex model for the infrared sector of SU(3) Yang-Mills theory – baryonic potential

M. Engelhardt¹

*Physics Department, New Mexico State University
Las Cruces, NM 88003, USA*

Abstract

The baryonic potential in the framework of the $SU(3)$ random vortex world-surface model is evaluated for a variety of static color source geometries. For comparison, carefully taking into consideration the string tension anisotropy engendered by the hypercubic lattice description, also the Δ and Y law predictions for the baryonic potential are given. Only the Y law predictions are consistent with the baryonic potentials measured.

PACS: 12.38.Aw, 12.38.Mh, 12.40.-y

Keywords: Center vortices, infrared effective theory, confinement, baryon potential

¹email: engel@nmsu.edu

1 Introduction

The random vortex world-surface model of the Yang-Mills vacuum [1, 2, 3, 4] is designed to describe the central phenomena induced by the strong interaction in the infrared regime: Confinement, spontaneous breaking of chiral symmetry, and the axial $U_A(1)$ anomaly. The motivation for the model is drawn from lattice Yang-Mills studies [5, 6, 7, 8, 9, 10, 11, 12, 13, 14] which suggest the relevance of center vortices for infrared strong interaction physics. For the case of $SU(2)$ color, the model has been shown to correctly predict (in the sense of agreement with corresponding lattice Yang-Mills results) a number of observables characterizing the aforementioned phenomena.

In a recent initial study of the generalization to $SU(3)$ color [4], the random vortex world-surface model was again found to reproduce the confinement properties of Yang-Mills theory. Both a low-temperature confining phase as well as a high-temperature deconfined phase are generated, separated by a weakly first order phase transition. The confinement properties are intimately related to the percolation properties of the vortices.

Apart from the order of the deconfining transition, a further aspect in which the $SU(3)$ theory differs substantially from the $SU(2)$ case is the long-range baryonic potential, which was not studied in [4]. This constitutes the subject of the present work. To arrive at definite statements concerning the baryonic potential, two issues must be taken into account. One issue is the breaking of spatial rotational symmetry in the present hypercubic lattice formulation of the model; after all, to measure baryonic potentials, it is necessary to evaluate Wilson loops which are not located within two-dimensional lattice planes. On the other hand, the Wilson loop areas spanned by baryonic configurations are substantially larger than the ones encountered in simple mesonic Wilson loop calculations; as a result, it is necessary to employ appropriate numerical noise reduction techniques to extract a meaningful signal for the baryonic potential. Having dealt with these two issues, the data collected in this work unequivocally point to a Y law for the baryonic potential as opposed to a Δ law, cf. Fig. 1. It should be noted that the form of the baryonic potential generated by vortex models has been the subject of recent debate [15, 16], and also within $SU(3)$ lattice Yang-Mills theory, the evidence in favor of the Y law at large separations has only been starting to outweigh the one in favor of the Δ law quite recently [17, 18, 19].

2 Model description

The random vortex world-surface model is based on the notion that the Yang-Mills vacuum is populated by random closed lines of quantized chromomagnetic flux (vortices), described by an ensemble of closed random world-surfaces in four-dimensional (Euclidean) space-time. In the present implementation of the model, these random surfaces are generated on a hypercubic lattice, composed of elementary squares on that lattice. The action governing the ensemble is related to the surface curvature: If two elementary squares which are part of a vortex surface share a lattice link but do not lie

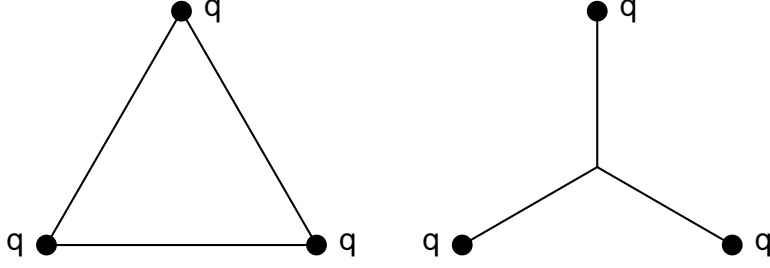


Figure 1: Based on the notion that three $SU(3)$ color sources in the Yang-Mills vacuum are bound by (linear) potentials associated with distances characterizing the spatial geometry of the sources, two distinct model bond topologies can be envisaged: The Δ law, where sources are connected pairwise (left), and the Y law, where bonds emanating from the sources meet at an (optimally placed) central junction (right). While the string tension in the Y law must be the same as in a mesonic configuration (where also a single bond emanates from each color source), the Δ model is assumed to be associated with half that string tension. This is based both on the short-distance perturbative limit and on the limit where two color sources approach each other, which should yield the usual mesonic string tension. Since in this limit, two of the bonds making up the Δ configuration merge, each of them is taken to contribute half of the mesonic string tension (this linear superposition of bonds constitutes an auxiliary model assumption which is not readily justified within the underlying nonabelian Yang-Mills theory, in which chromoelectric flux tubes interact nontrivially when approaching each other).

in the same plane, this costs an action increment c . Formally, this can be written as a sum over lattice links,

$$\begin{aligned}
S[q] = c \sum_x \sum_\mu \left[\sum_{\substack{\nu < \lambda \\ \nu \neq \mu, \lambda \neq \mu}} (|q_{\mu\nu}(x) q_{\mu\lambda}(x)| + |q_{\mu\nu}(x) q_{\mu\lambda}(x - e_\lambda)| \right. \\
\left. + |q_{\mu\nu}(x - e_\nu) q_{\mu\lambda}(x)| + |q_{\mu\nu}(x - e_\nu) q_{\mu\lambda}(x - e_\lambda)|) \right] \\
= \frac{c}{2} \sum_x \sum_\mu \left[\left[\sum_{\nu \neq \mu} (|q_{\mu\nu}(x)| + |q_{\mu\nu}(x - e_\nu)|) \right]^2 - \sum_{\nu \neq \mu} [|q_{\mu\nu}(x)| + |q_{\mu\nu}(x - e_\nu)|]^2 \right],
\end{aligned} \tag{1}$$

where $q_{\mu\nu}(x)$ describes the chromomagnetic flux associated with the elementary square extending from the site x into the positive μ and ν directions. In the $SU(3)$ model, the variables $q_{\mu\nu}(x)$ can take three values, $q_{\mu\nu}(x) \in \{-1, 0, 1\}$; the value 0 indicates that the elementary square is not part of a vortex surface, whereas the values ± 1 indicate that it is. The latter two values distinguish the two possible types of quantized flux carried by $SU(3)$ vortices. These will be characterized in detail in the next section by their effect on Wilson loops circumscribing them. Note that S is symmetric with respect to the two possible types of vortex flux. Note furthermore that, formally, there are two variables connected with the elementary square extending from the site x into the positive μ and ν directions, namely $q_{\mu\nu}(x)$ and $q_{\nu\mu}(x)$; these correspond to the two opposite orientations, i.e. senses of curl, one may ascribe to a surface. However, since both variables are meant to describe the same flux (which, apart from its location in space-time, also carries a

definite orientation), they are related by² $q_{\mu\nu}(x) = -q_{\nu\mu}(x)$.

It should also be emphasized that the vortex ensemble is generated subject to the constraint of continuity of flux (modulo 2π , i.e. modulo Dirac strings [2, 3, 4]). For one, this forces vortex surfaces to be closed, as already mentioned above; on the other hand, the existence of two types of quantized flux in the $SU(3)$ model nevertheless allows for vortex branchings, where a vortex of one type splits into two vortices of the other type while maintaining continuity of flux³. As described in detail in [4], continuity of flux in practice is guaranteed during the generation of the vortex world-surface ensemble by performing updates simultaneously on the six squares making up the surface of an elementary three-dimensional cube in the lattice. This is done in a way which corresponds to superimposing the (continuous) flux of a vortex of the shape of the elementary cube surface onto the flux previously present.

The flux world-surfaces defined in this manner are formally infinitely thin; however, they are meant to describe physical vortex structures present in the Yang-Mills vacuum which possess a finite transverse thickness, akin to the structures making up the Copenhagen vacuum [21]. The model surfaces represent the geometrical centers of such physical thick vortices. The thickness enters the model description through the spacing of the lattice on which the vortex surfaces are generated. For instance, two parallel physical vortices can only be meaningfully distinguished from one another when they are further apart than a minimal distance. In the model, this distance is encoded in the lattice spacing; at shorter distances, the thick structures cannot be distinguished and thus should be represented instead by a single model world-surface of combined flux. For a thorough discussion of the role of the lattice spacing in the random vortex world-surface model, cf. [1, 4].

Given this definite physical meaning of the lattice spacing, it follows that it is a fixed finite quantity in the model⁴, which should be contrasted with conventional lattice gauge theory, where one is ultimately interested in the limit of vanishing lattice spacing. This has consequences as far as the breaking of spatial rotational symmetry by the underlying hypercubic lattice structure is concerned. Whereas in lattice gauge theory, spatial rotational symmetry is restored in the course of taking the continuum limit [22], in the random vortex world-surface model the breaking of rotational symmetry engendered by the hypercubic lattice description and manifest in the action (1) is a real model property which will be quantified in detail in section 5. Roughly, string tensions along diagonal directions in the lattice are enhanced compared with the one measured along lattice axes to the extent that the most extreme string tension values obtained are

²Note that, in light of the description above, this (correctly) implies that a vortex carrying one type of flux is equivalent to an oppositely oriented vortex carrying the other type of flux for the present purposes (namely, for evaluating Wilson loops). Indeed, these two cases only differ by a flux 2π , i.e. a Dirac string, which is unobservable in Wilson loops. On the other hand, when considering topological properties [20, 2], the two cases do have to be distinguished and one cannot trade off geometrical orientation of a vortex in space-time against the magnitude of flux it carries.

³This does not happen in the $SU(2)$ model, which only has one type of flux, corresponding to the existence of only one nontrivial element in the center of the $SU(2)$ group.

⁴This should also be expected from the point of view that the random vortex world-surface model is an infrared effective model, which is only defined up to a fixed ultraviolet cutoff.

separated from their mean by 13 %. This variation must be taken into account when comparing baryonic potentials with Δ or Y law expectations.

It should be noted that, while the random vortex world-surface model is intended to be more than just a qualitative model of strong interaction physics, on a quantitative level it is generally not expected to furnish a description of medium- to long-range observables better than to within of the order of 10 %. After all, it encodes a truncated dynamics in which phenomena such as the Coulomb potential between color sources are missing and effects at distances shorter than about 0.4 fm cannot be resolved. In light of this, the consequences of the hypercubic realization of the random vortex surfaces, which include the breaking of spatial rotational symmetry discussed above, represent just one particular model distortion of reality among others. No more (or less) significance needs to be attached to this specific distortion than to others on a similar quantitative level, such as ambiguities in measurements of the topological susceptibility [2] and of the quenched chiral condensate [3]. Note also that the breaking of rotational symmetry is only introduced by the particular (technically convenient) hypercubic lattice implementation of the model; a manifestly symmetric random vortex world-surface model could e.g. be formulated using randomly triangulated surfaces in continuous four-dimensional space-time.

3 Observables

Physically, the random vortex surfaces represent quantized chromomagnetic flux. This means that they contribute in a characteristic way to Wilson loops; if one chooses an area spanning a given Wilson loop⁵, then for each time a vortex world-surface pierces⁶ that area, the Wilson loop acquires a phase factor corresponding to the center of the gauge group. For the case of $SU(3)$ color, there are two possible phase factors, associated with the two possible types of quantized vortex flux, namely $\exp(\pm i2\pi/3)$. To be precise, consider an elementary Wilson loop (plaquette) extending from y into the positive κ and λ directions, with the integration oriented such that one starts at y , integrates first into the positive κ direction, and then onwards around the plaquette. Denote this by $U_{\kappa\lambda}(y)$. The plaquette $U_{\kappa\lambda}(y)$ is pierced precisely by the dual lattice elementary square $q_{\mu\nu}(x)$, where the indices $\kappa, \lambda, \mu, \nu$ span all four space-time dimensions and $x = y + (\vec{e}_\kappa + \vec{e}_\lambda - \vec{e}_\mu - \vec{e}_\nu)a/2$, with a denoting the lattice spacing. $U_{\kappa\lambda}(y)$ can thus be given exclusively in terms of the corresponding $q_{\mu\nu}(x)$, namely

$$U_{\kappa\lambda}(y) = \exp(i\pi/3 \cdot \epsilon_{\kappa\lambda\mu\nu} q_{\mu\nu}(x)) \quad (2)$$

(with the usual Euclidean summation convention over Greek indices).

To evaluate an arbitrary Wilson loop, it is sufficient [4] to find a tiling of that Wilson loop by a set of plaquettes and multiply the values those plaquettes take in the given

⁵The choice of area is immaterial due to the continuity of flux.

⁶Note that Wilson loops are defined on a lattice dual to the one on which the vortices are defined, i.e. on a lattice shifted by the vector $(a/2, a/2, a/2, a/2)$, where a denotes the lattice spacing. Thus, the notion of a vortex piercing a Wilson loop area is unambiguous.

vortex configuration, as specified by (2).

Consider now a baryonic Wilson loop,

$$W = \frac{1}{6} \epsilon_{abc} \epsilon_{a'b'c'} \Gamma_1^{aa'} \Gamma_2^{bb'} \Gamma_3^{cc'} \quad (3)$$

where Γ_i denotes the path-ordered exponential (Wilson) line integral along the path taken by the i -th color source. All three Γ_i start at the same initial space-time point and end at the same final space-time point. Due to the special properties of center vortex configurations, the baryonic Wilson loop in such configurations can be straightforwardly decomposed into three standard mesonic Wilson loops. On the one hand, any center vortex configuration can be written in terms of gauge fields defined purely within the (Abelian) Cartan subgroup of the underlying gauge group [20]. Under these circumstances, the Γ_i in (3) are diagonal, and by multiplying (3) with the (unit) determinant of another color matrix Γ_0 given by an additional exponential line integral connecting the end point of the Γ_i with their initial point,

$$1 = \Gamma_0^{11} \Gamma_0^{22} \Gamma_0^{33} \quad (4)$$

one can rewrite the baryonic Wilson loop as

$$W = \frac{1}{6} \sum_{a,b,c} \epsilon_{abc}^2 (\Gamma_1^{aa} \Gamma_0^{aa}) (\Gamma_2^{bb} \Gamma_0^{bb}) (\Gamma_3^{cc} \Gamma_0^{cc}) \quad (5)$$

On the other hand, since in a center vortex configuration, the exponential integral along a path with coinciding initial and final points is proportional to the unit matrix (this is the defining property of center flux), this indeed is equal to a product of three standard mesonic Wilson loops,

$$W = \left(\frac{1}{3} \text{Tr} \Gamma_1 \Gamma_0 \right) \left(\frac{1}{3} \text{Tr} \Gamma_2 \Gamma_0 \right) \left(\frac{1}{3} \text{Tr} \Gamma_3 \Gamma_0 \right) \quad (6)$$

In practice, in the present work, the baryonic correlator of three Polyakov loops was evaluated. This is of course nothing but a special case of the baryonic Wilson loop discussed above, with paths Γ_i starting from an initial spatial position x_0 at time $t = 0$, running to spatial positions x_i while at $t = 0$, remaining there as time runs through the complete extension of the lattice to the final time $t = \beta$ (which is identified with $t = 0$, with periodic boundary conditions on the gauge fields), and returning to x_0 along the same path as they took at $t = 0$. Due to the Abelian nature of the vortex gauge fields, all the line integrals at $t = 0$ and $t = \beta$ cancel and one is left with a baryonic Polyakov loop correlator. In accordance with the discussion above, this is furthermore equal to the expectation value of a product of three standard mesonic Polyakov loop pairs such as the ones used to evaluate standard mesonic Polyakov loop correlators. The baryonic Polyakov loop correlator observable has the advantage that boundary effects resulting from the propagation of the color sources from x_0 to x_i and back cancel; on the other hand, it limits the temporal extension of the lattice universe one can achieve without losing the baryonic Wilson loop signal to numerical noise⁷.

⁷Corresponding to this treatment of the baryonic potential, also the mesonic string tension will be evaluated in section 5 using Polyakov loop correlators.

4 Numerical noise reduction

To nevertheless reduce the numerical noise contaminating the mesonic and baryonic Polyakov loop correlator measurements as far as possible, the noise reduction technique introduced by Lüscher and Weisz [23] was employed. Given an action which can be decomposed as

$$S[q] \equiv S[q^t, q^s] = S^t[q^t] + \sum_i S^i[q^t, q_i^s], \quad (7)$$

an observable O which correspondingly factorizes as

$$O[q] \equiv O[q^t, q^s] = \prod_i O^i[q^t, q_i^s], \quad (8)$$

and a constraint δ which separates as

$$\delta[q] \equiv \delta[q^t, q^s] = \delta^t[q^t] \prod_i \delta^i[q^t, q_i^s], \quad (9)$$

the method of Lüscher and Weisz corresponds to evaluating the expectation value of O over the set of variables q subject to the constraint δ using the action S as

$$\begin{aligned} \langle O \rangle_{\{q; \delta; S\}} &= \frac{1}{Z} \int [Dq^t] \delta^t[q^t] \exp(-S^t[q^t]) \prod_i \int [Dq_i^s] \delta^i[q^t, q_i^s] O^i[q^t, q_i^s] \exp(-S^i[q^t, q_i^s]) \\ &= \left\langle \prod_i \langle O^i \rangle_{\{q_i^s; \delta^i; S^i\}}[q^t] \right\rangle_{\{q; \delta; S\}} \end{aligned} \quad (10)$$

In other words, the variables q^t are kept fixed while the inner expectation values are taken over their respective variables q_i^s using the actions S^i subject to the constraints δ^i ; in the outer averaging over the full set of variables q subject to the full constraint δ using the full action S , the product of these inner expectation values may be much easier to sample than the original $O[q^t, q^s]$ was. Note that, in practice, this method often can be iterated in the sense that one may again select from the set of variables q^t a subset which is to be kept fixed while its complement is being used for averaging; as long as the action, the constraint and the quantity being averaged can be decomposed in analogy to (7)-(9), one can construct additional hierarchies of averaging, where the quantities being averaged at each level only depend on a subset of the variables the quantities at the next-lower level depended on.

This method applies to the random vortex world-surface model if one chooses as the variables q^t all elementary squares which extend into the time and one space direction, and as the variables q_i^s the elementary squares at the i -th lattice time (which extend into two spatial directions). The action (1) is a sum over terms associated with lattice links, each term coupling only elementary squares attached to the corresponding link. The sum over spatial links at the i -th lattice time thus yields the S^i piece of the action, whereas the sum over all temporal links yields the S^t piece. Similarly, the constraint of continuity of flux is to be satisfied independently at each lattice link [4] by the elementary squares attached to that link; it thus factorizes into terms coupling only the variables q^t and q_i^s

at fixed i , as well as a term constraining only the variables q^t . Lastly, any Wilson loop can be evaluated as a product over single plaquettes, which in turn each only depend on the value of a single vortex elementary square according to (2); this can thus be trivially grouped into factors satisfying the factorization (8). In accordance with the remarks on the update procedure in section 2, in this first level of averaging, elementary updates are thus only performed on surfaces of elementary lattice cubes which lie in a fixed time slice, i.e., which extend into three spatial directions.

After this decomposition, in practice also a second averaging hierarchy was employed; namely, the set of elementary squares q^t extending into the time and one space direction was decomposed into sets of squares q_{2i}^t connecting the $(2i - 1)$ -th lattice time with the $(2i)$ -th lattice time, with the remaining elementary squares making up the set \bar{q}^t to be kept fixed at this second level of averaging. With this decomposition, the properties (7)-(9) are again satisfied; note that, for fixed i , the variables q_{2i}^t only enter the product of inner expectation values

$$\langle O^{2i-1} \rangle_{\{q_{2i-1}^s; \delta^{2i-1}; S^{2i-1}\}} \langle O^{2i} \rangle_{\{q_{2i}^s; \delta^{2i}; S^{2i}\}} .$$

Thus, in this second level of averaging, updates were performed on the surfaces of all elementary lattice cubes except for the ones connecting even lattice times $2i$ with the next *higher* odd lattice times $2i + 1$.

In practice, it turned out to be efficient to carry out the innermost averaging using either 4000 or 8000 configurations; in the second-level averaging, either 200 or 400 configurations were used. For the outermost averaging, typically 20 to 60 configurations were enough to achieve a sufficient level of accuracy.

5 Angular dependence of the string tension

As already mentioned further above, the mesonic string tension was evaluated using Polyakov loop correlators, employing the noise reduction techniques discussed in the previous section. In practice, $16^3 \times 4$ lattices were used, with the curvature coupling c in (1) set to the physical value $c = 0.21$, cf. [4]. The temporal extension of four lattice spacings corresponds to a temperature of $T = 0.45T_c$ (where T_c denotes the deconfinement temperature). In the case of the static potential between sources separated along one of the lattice axes studied in [4], the string tension at this temperature deviated from the extrapolation to zero temperature by less than 1 %.

The mesonic geometries studied in the present work are listed in Table 1. The geometry labels defined there will be used below to refer to the different cases. String tensions σ were extracted by fitting the behavior of the measured Polyakov loop correlators $P(nda)$ at different spatial distances nda separating the Polyakov loops by the ansatz

$$\frac{-\ln P(nda)}{4anda} = \sigma + \frac{\tau}{n} \quad (11)$$

Geometry label	Relative spatial separation of Polyakov loops	Scale factors n used	String tension in lattice units σa^2
$M100$	$n \cdot (a, 0, 0)$	1, 2, 3, 4, 5	0.7659 ± 0.0004
$M110$	$n \cdot (a, a, 0)$	1, 2, 3	0.907 ± 0.001
$M210$	$n \cdot (2a, a, 0)$	1, 2	$0.885^{+0.001}_{-0.027}$
$M310$	$n \cdot (3a, a, 0)$	1, 2	$0.83^{+0.015}_{-0.04}$
$M111$	$n \cdot (a, a, a)$	1, 2	$1.02^{+0.002}_{-0.035}$
$M211$	$n \cdot (2a, a, a)$	1, 2	$0.974^{+0.001}_{-0.03}$

Table 1: Mesonic geometries and associated string tensions.

using the $n = 1, 2$ data, where a denotes the lattice spacing⁸. Of course, $4a$ is the temporal extension of the lattice, cf. above; thus, the denominator on the left hand side is simply the minimal area spanned by the pair of Polyakov loops. The accuracy of this procedure was checked by also performing fits of the form $\sigma + \tau/n + \rho/n^2$ to the $n = 1, 2, 3$ data in the $M100$ and $M110$ cases; this led to adjustments of the string tension values by at most 3 % (in both cases, downwards). These fits then did also describe the $n = 4, 5$ data in the $M100$ case within their statistical errors. In the error analysis of quantities derived from string tensions extracted using only $n = 1, 2$ data, the aforementioned 3 % systematical downwards uncertainty in these string tensions is incorporated. The string tensions are listed in Table 1.

Whereas Δ law predictions for the baryonic configurations studied further below can be made purely on the basis of σ_{M100} and σ_{M110} , to arrive at Y law predictions, it is necessary to interpolate continuous angular dependences of the mesonic string tension from the discrete string tension data collected. To be specific, it is necessary to combine σ_{M100} , σ_{M310} , σ_{M210} and σ_{M110} to interpolate the string tension for two sources separated along the direction $(\cos \alpha, \sin \alpha, 0)$, and to combine σ_{M100} , σ_{M211} and σ_{M111} to interpolate the string tension for two sources separated along the direction $((1/\sqrt{2}) \sin \beta, (1/\sqrt{2}) \sin \beta, \cos \beta)$. Since the functional form of the α - and β -dependences is unknown, the quite conservative corridors for these dependences depicted in Fig. 2 were allowed for. Error bars for Y law predictions below are based on the extremes allowed by these corridors.

6 Baryonic geometries

Baryonic potentials were measured by evaluating baryonic Polyakov loop correlators as discussed in section 3. As in the mesonic case, $16^3 \times 4$ lattices were used at the physical

⁸In physical units, obtained [4] by equating the zero-temperature string tension (along lattice axes) with $(440 \text{ MeV})^2$, the lattice spacing in the random vortex world-surface model is 0.39 fm.

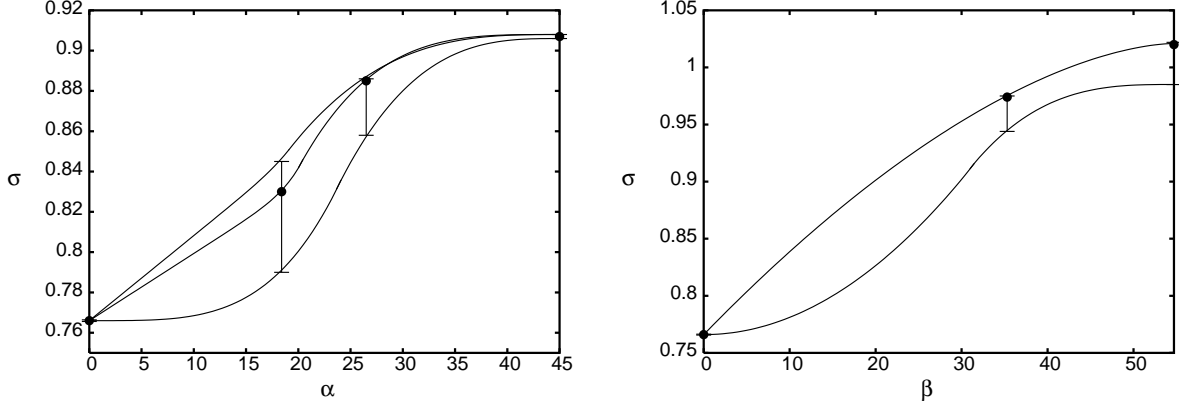


Figure 2: Angular dependence of the string tension σ . Left panel: As a function of the angle α when the static sources are separated along the direction $(\cos \alpha, \sin \alpha, 0)$; right panel: As a function of the angle β when the static sources are separated along the direction $((1/\sqrt{2}) \sin \beta, (1/\sqrt{2}) \sin \beta, \cos \beta)$. Curves are fitted to the measured string tension values and to the extreme values allowed by their error bars. In the case of $\sigma(\beta)$, the fit to the measured values and the upper extreme coincide within the resolution of the plot.

point $c = 0.21$. Table 2 lists the baryonic geometries studied⁹.

Geometry label	Static quark positions	Scale factors n used	Baryonic tension in lattice units Va^2
BL	$(0, 0, 0)$ $n \cdot (a, 0, 0)$ $n \cdot (0, a, 0)$	1, 2, 3	1.518 ± 0.002
BT	$n \cdot (0, a, 0)$ $n \cdot (a, 0, 0)$ $n \cdot (-a, 0, 0)$	1, 2	$2.29^{+0.002}_{-0.07}$
BS	$n \cdot (a, 0, 0)$ $n \cdot (0, a, 0)$ $n \cdot (0, 0, a)$	1, 2	$2.276^{+0.005}_{-0.073}$

Table 2: Baryonic geometries and associated baryonic tensions.

Similar to the mesonic case, the leading long-range behavior of the potential was extracted by fitting the measured baryonic Polyakov loop correlators P_n^B at the scale factors n by the ansatz

$$\frac{-\ln P_n^B}{4ana} = V + \frac{U}{n} \quad (12)$$

using the $n = 1, 2$ data. The baryonic tension V can thus be directly compared to

⁹The geometry labels BL, BT, BS originate from the author's subjective picturing of the respective configurations as “L-shaped”, “T-shaped” and “symmetric”.

Δ and Y law predictions obtained by adding bond lengths (in units of na) weighted by the associated string tensions σ . In the BL case, fitting the $n = 1, 2, 3$ data by $V + U/n + W/n^2$ led to a downwards adjustment of V by 1.25 %. The baryonic tensions V are listed in Table 2. Motivated by the results of the fits in the mesonic case, the baryonic tensions extracted using only $n = 1, 2$ data were again also endowed with a 3 % downwards systematic uncertainty.

Δ law predictions for these baryonic configurations are quite straightforward, since the only relevant bond string tensions are $\sigma_{M100}/2$ and $\sigma_{M110}/2$ (the reader is reminded that the Δ model assumes half the mesonic string tensions to be associated with the bonds). The predictions are

$$V_{BL}^{\Delta} a^2 = 2(\sigma_{M100} a^2/2) + \sqrt{2}(\sigma_{M110} a^2/2) = 1.407 \pm 0.001 \quad (13)$$

$$V_{BT}^{\Delta} a^2 = 2\sqrt{2}(\sigma_{M110} a^2/2) + 2(\sigma_{M100} a^2/2) = 2.0485 \pm 0.0015 \quad (14)$$

$$V_{BS}^{\Delta} a^2 = 3\sqrt{2}(\sigma_{M110} a^2/2) = 1.924 \pm 0.002 \quad (15)$$

On the other hand, to arrive at Y law predictions, one must perform a potential energy minimization as a function of the bond junction position; the interplay of varying bond lengths and associated string tensions may favor a different bond junction than the one which would be favorable if the string tension were perfectly isotropic. Since the string tension is enhanced along diagonal directions, the optimal bond geometry will be more aligned with the lattice axes than in the isotropic case. Exploring bond junction positions in the spatial 1-2-plane for the BL and BT configurations and minimizing the associated potential energy for the range of angular dependences $\sigma(\alpha)$ depicted in Fig. 2, one arrives at the Y law predictions

$$V_{BL}^Y a^2 = 1.523 \pm 0.008 \quad (16)$$

$$V_{BT}^Y a^2 = 2.25^{+0.02}_{-0.08} . \quad (17)$$

Specifically, the expectation is determined by using for $\sigma(\alpha)$ the fit to the measured string tension values displayed in Fig. 2, whereas the error bars are determined by using the most extreme $\sigma(\alpha)$ dependences allowed for by Fig. 2.

Treatment of the BS geometry is more complicated. If one assumes the 60° discrete rotational symmetry of the configuration to be unbroken, then the bond junction position is located in the $(1, 1, 1)$ direction viewed from the origin and one can straightforwardly use the range of angular dependences $\sigma(\beta)$ allowed for by Fig. 2 to analyze this restricted case, in complete analogy to the treatment of the BL and BT configurations above. Searching for the minimal potential energy under this assumption to arrive at a first estimate regarding the Y law prediction for the BS geometry, one arrives at

$$V_{BS}^Y a^2 \Big|_{(1,1,1)} = 2.271^{+0.002}_{-0.18} . \quad (18)$$

On the other hand, there is no guarantee that the bond junction will indeed be located in the $(1, 1, 1)$ direction viewed from the origin. It is therefore necessary to explore the whole three-dimensional range of possible bond junction positions; however, the associated potential energies in general can only be given if the general angular dependence

of the string tension is supplied. To arrive at an estimate for this dependence, the particular cases $\sigma(\alpha)$ and $\sigma(\beta)$ displayed in Fig. 2, which essentially give the string tension at 0° and 45° longitude on a sphere (if one additionally uses $\sigma(\beta = 90^\circ) = \sigma(\alpha = 45^\circ)$), were used to construct an interpolation of the string tension for other longitudes φ . To be specific, the form $\sigma(\varphi) = (1 - \sin(2\varphi))\sigma(\varphi = 0^\circ) + \sin(2\varphi)\sigma(\varphi = 45^\circ)$ was assumed, which also reasonably well fits the additional information that the dependence on the longitude φ at the “equator”, i.e., connecting $\sigma(\alpha = 90^\circ)$ with $\sigma(\beta = 90^\circ)$, must again take the same functional form as $\sigma(\alpha)$. This interpolation was carried out both for the fits to the measured string tension values in Fig. 2 as well as for the upper and lower extremes, in order to again arrive at an error estimate for the Y law generated. On this basis, exploring the whole three-dimensional range of possible bond junction positions indeed yields a slightly more favorable asymmetric bond junction position and an associated Y law prediction of

$$V_{BS}^Y a^2 = 2.25_{-0.16}^{+0.02} \quad (19)$$

which only deviates little from (18); in analogy to above, the error bars are based on minimizing the potential energy using the φ -interpolations of the extreme $\sigma(\alpha)$ and $\sigma(\beta)$ dependences allowed for by Fig. 2. Thus, the systematic error associated with restricting the range of bond junction positions in arriving at (18) appears to be comparatively minor.

7 Conclusions

Carefully taking into account the anisotropy in the string tension introduced into the random vortex world-surface model by the hypercubic treatment of the vortex surfaces, one obtains an unambiguous characterization of the behavior of the baryonic potential. Assembling the measured potentials and the corresponding Δ and Y law predictions from the previous section, cf. Table 3, it is evident that the Δ law does not agree with

Geometry	Va^2	$V^Y a^2$	$V^\Delta a^2$
<i>BL</i>	1.518 ± 0.002	1.523 ± 0.008	1.407 ± 0.001
<i>BT</i>	$2.29_{-0.07}^{+0.002}$	$2.25_{-0.08}^{+0.02}$	2.0485 ± 0.0015
<i>BS</i>	$2.276_{-0.073}^{+0.005}$	$2.25_{-0.16}^{+0.02}$	1.924 ± 0.002

Table 3: Comparison of measured baryonic tensions with Δ and Y law predictions.

the measured baryonic potential, whereas the Y law yields rather accurate predictions for it. It should be noted that the Y law behavior is seen quite clearly already at moderate distances in the vortex model, contrary to full lattice Yang-Mills theory [19], where it is necessary to consider rather large distances. In the full theory, presumably the short-distance perturbative Δ behavior masks the long-distance Y law and pushes its onset to larger separations. In the vortex model, by contrast, such perturbative effects

are truncated and the Y law induced by the vortices clearly dominates the behavior of the baryonic potential.

Acknowledgments

The author is grateful to M. Quandt and H. Reinhardt for fruitful discussions on the $SU(3)$ random vortex world-surface model, and to P. de Forcrand for enlightening correspondence on aspects of the baryonic potential. Furthermore, science+computing ag, Tübingen, is acknowledged for providing computational resources. This work was supported in part by the U.S. DOE under grant number DE-FG03-95ER40965.

References

- [1] M. Engelhardt and H. Reinhardt, Nucl. Phys. **B585** (2000) 591.
- [2] M. Engelhardt, Nucl. Phys. **B585** (2000) 614.
- [3] M. Engelhardt, Nucl. Phys. **B638** (2002) 81.
- [4] M. Engelhardt, M. Quandt and H. Reinhardt, Nucl. Phys. **B685** (2004) 227.
- [5] L. Del Debbio, M. Faber, J. Greensite and Š. Olejník, Phys. Rev. **D 55** (1997) 2298.
- [6] L. Del Debbio, M. Faber, J. Giedt, J. Greensite and Š. Olejník, Phys. Rev. **D 58** (1998) 094501.
- [7] M. Faber, J. Greensite and Š. Olejník, Phys. Lett. **B474** (2000) 177.
- [8] J. Greensite, Prog. Part. Nucl. Phys. **51** (2003) 1.
- [9] R. Bertle, M. Engelhardt and M. Faber, Phys. Rev. **D 64** (2001) 074504.
- [10] K. Langfeld, O. Tennert, M. Engelhardt and H. Reinhardt, Phys. Lett. **B452** (1999) 301.
- [11] M. Engelhardt, K. Langfeld, H. Reinhardt and O. Tennert, Phys. Rev. **D 61** (2000) 054504.
- [12] P. de Forcrand and M. D’Elia, Phys. Rev. Lett. **82** (1999) 4582.
- [13] C. Alexandrou, M. D’Elia and P. de Forcrand, Nucl. Phys. Proc. Suppl. **83** (2000) 437.
- [14] P. de Forcrand and M. Pepe, Nucl. Phys. **B598** (2001) 557.
- [15] J. M. Cornwall, Phys. Rev. **D 54** (1996) 6527.

- [16] J. M. Cornwall, Phys. Rev. **D 69** (2004) 065013.
- [17] T. T. Takahashi, H. Matsufuru, Y. Nemoto and H. Suganuma, Phys. Rev. Lett. **86** (2001) 18;
T. T. Takahashi, H. Suganuma, Y. Nemoto and H. Matsufuru, Phys. Rev. **D 65** (2002) 114509.
- [18] C. Alexandrou, P. de Forcrand and A. Tsapalis, Phys. Rev. **D 65** (2002) 054503.
- [19] C. Alexandrou, P. de Forcrand and O. Jahn, Nucl. Phys. Proc. Suppl. **119** (2003) 667.
- [20] M. Engelhardt and H. Reinhardt, Nucl. Phys. **B567** (2000) 249.
- [21] H. B. Nielsen and P. Olesen, Nucl. Phys. **B160** (1979) 380;
J. Ambjørn and P. Olesen, Nucl. Phys. **B170** [FS1] (1980) 60;
J. Ambjørn and P. Olesen, Nucl. Phys. **B170** [FS1] (1980) 265.
- [22] J. B. Kogut, Rev. Mod. Phys. **55** (1983) 775.
- [23] M. Lüscher and P. Weisz, JHEP **0109** (2001) 010.